Analysis of small scale fluctuations in Hall effect thrusters using virtual Thomson scattering on PIC simulations

Tarek Ben Slimane, Cyrille Honoré, Thomas Charoy, Anne Bourdon, Pascal Chabert

Analysis of small scale fluctuations in Hall effect thrusters using virtual Thomson scattering on PIC simulations

Tarek Ben Slimane,[1, a)] Cyrille Honoré,[1] Thomas Charoy,[1] Anne Bourdon,[1] and Pascal Chabert[1]

Laboratoire de Physique des Plasmas (LPP), CNRS, Sorbonne Université, École Polytechnique, Institut Polytechnique de Paris, 91120 Palaiseau, France

(Dated: 10 January 2022)

Hall effect thrusters are yet not fully understood due to multiple open questions, among which the anomalous electron transport is the most challenging. Particle-In-Cell (PIC) simulations suggested that electron transport is strongly affected by small-scale instabilities which can be investigated experimentally using Collective Thomson Scattering (CTS). In this paper, we perform a virtual CTS diagnostic on PIC data in order to investigate these small scales and to relate simulation and experiments. The virtual diagnostic is performed on the electron density maps from a simplified 2D axial-azimuthal PIC simulation. Analysis along the channel axis showed two dominant modes at $8\,\mathrm{rad.mm^{-1}}$ and $3\,\mathrm{rad.mm^{-1}}$. These modes exhibit ion-acoustic wave features and appear to be selectively affected by the acceleration of the ions when transitioning from the ionization zone to the acceleration zone. A numerical study of the electron density fluctuation rate from the virtual CTS is also performed and the obtained profiles are compared to PIC. This reveals that the virtual CTS integrates both axial and azimuthal fluctuations of the electron density due to the spatial extension of the scattering volume. Moreover, it also highlights the importance of a good estimation of the electron density in the scattering volume for an accurate estimation of the fluctuation rate.

PACS numbers: 0

[a)]tarek.ben-slimane@lpp.polytechnique.fr

I. INTRODUCTION

Since their development in the mid-60s, Hall effect thrusters (HET) have been successfully used for many space missions either as a secondary propulsion system destined for station keeping and attitude control or as a primary propulsion system for interplanetary missions[1,2]. The propellant, commonly a noble gas, is injected from the anode side into an annular chamber while an electron-emitting cathode provides electrons to ionize the propellant and produce plasma. A high voltage is applied across the chamber and accelerates ions downstream while electrons are trapped in a $E \times B$ configuration using a strong radial magnetic field. However, the rate at which electrons flow from the cathode to the anode exceeds the rates predicted by classical theory by several orders of magnitude, which impede a full understanding of HET operation.

Several contributions to this anomalous mobility have been extensively studied throughout the years[3–5] and recently the electron cyclotron drift instability or ECDI was identified as a key driver for electron transport. Indeed, the asymmetry between the electron fast azimuthal motion and the ions' axial motion creates a kinetic, MHz (millimeter scale) azimuthal instability that was observed in PIC simulations[6–10] as well as in experiments[11–15] and was associated with enhanced electron transport. The linear theory of ECDI instability is well developed, however, nonlinear saturation is still the subject of active research and debate as discussed in the recent review by Kaganovich *et al.*[16]. Given the complexity of mode saturation in the 3D geometry of Hall thrusters, only large-scale 3D PIC simulations can provide a full understanding of the mechanism of anomalous transport. However, these simulations are still out of reach and most PIC simulation studies are carried out in simplified 1D and 2D configurations.

Experimentally, the investigation of instabilities at millimeter scales in a 3D thruster is challenging and was done so far using coherent Thomson scattering (CTS)[13,17–19] and different probe techniques[12,15,16]. Furthermore, most measurements are performed outside the narrow thruster channel, in the vicinity of the exit plane, and downstream in the plume.

In 2011, a previous work by Honoré et al.[20] used an analysis method that combines 2D PIC axial-azimuthal simulation results with a virtual CTS. The approach consisted of generating a theoretical scattering signal from PIC data and showed an excellent agreement with CTS observations of the plume on the static form factor which is a measure of the intensity of the electron density fluctuations. However, the time resolution of the PIC simulation used was limited to $\Delta t = 1\,\mu$s so that no spectral comparison was performed.

In this paper, we apply a virtual CTS method to the highly resolved PIC simulations of a 2D PIC axial-azimuthal benchmark test case developed recently in Ref.[10] to identify the main parameters impacting the evaluation of the electron density fluctuation rate between PIC simulations and CTS experiments. This is achieved by comparing the reference fluctuation rate derived from PIC data with the one obtained from virtual CTS analysis.

CTS experiments usually measure an electron density fluctuation rate of the order of 1%[17], whereas PIC simulations tend to produce large electron density fluctuations at around 10%-15% with significant axial variations[8]. This difference is often explained by stating that, as aforementioned, 2D simulations are unable to account for the 3D structure of the ECDI. Nevertheless, experiment-wise, the determination of the absolute electron fluctuation rate in CTS is also challenging since it requires a precise measurement of the electron density in the scattering volume and absolute calibration of the setup[21]. Still, recent work using incoherent Thomson scattering to measure this density reported a local electron density lower than previous estimates and a fluctuation density rate of the order of 8%[22], closer to the value reported by simulations.

In this respect, the local electron density inside the scattering volume seems to have a significant impact on the value of the fluctuation rate. The probed volume, which is defined by the intersection of two laser beams, depends on the waist of the laser. Experimentally, it is very burdensome to vary this parameter and keep a good-quality signal, since it directly impacts the measurement resolution. On the other hand, since PIC simulations are only limited by the mesh resolution, it is possible to numerically produce the scattering signal from PIC data for different waists and assess the impact of the waist on the estimation of the electron density fluctuation rate. Furthermore, PIC results offer more flexibility in terms of the accessible zones for the diagnostic. Indeed, contrary to CTS experiments where the diagnostic has only been done outside the thruster channel, by basing a virtual CTS on PIC results, it is also possible to explore the thruster channel. Interestingly, a similar virtual diagnostic was also performed within an incoherent Thomson scattering setup in Ref.[23] to investigate the impact of the laser intensity on the measurement of the electron density. The study also highlighted the valuable flexibility and insight that virtual diagnostics can bring to experiments.

The organization of the paper is as follows. The 2D axial-azimuthal PIC simulation and the virtual collective Thomson scattering analysis are presented in Section II. Then, in section III, first, we present the virtual CTS observation at a fixed time to identify the dominant modes in the plume as well as in the thruster channel. Then, we perform a temporal-Fourier analysis to

identify the main frequencies and derive the dispersion relations for the dominant propagating modes. Finally, we discuss the impact of the waist of laser beams on the derivation of electron density fluctuations.

II. METHODS

A. Axial-Azimuthal PIC Simulation

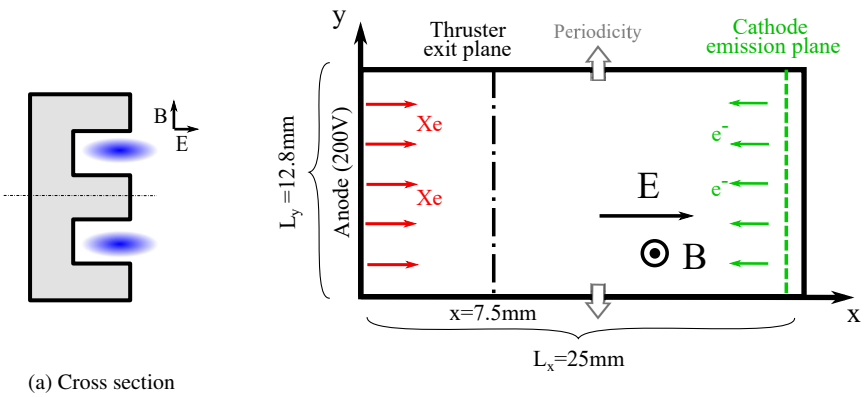

(a) Cross section

(b) Simulation domain

FIG. 1: Schematic of a transversal cross-section of the thruster and the simulation domain adapted from Ref[10]. x is the axial direction, y is the (periodic) azimuthal direction. Black dashed line at $x = 7.5\,\text{mm}$ corresponds to the position of the maximum radial magnetic field and the exit plane of the thruster. Green dashed line at $x = 24\,\text{mm}$ is the plane from which electrons are emitted.

As mentioned in the introduction, an absolute comparison with CTS experimental results would require a full highly-resolved 3D PIC simulation of the whole thruster. However, the latter is still out of reach due to its computational cost. Currently, 2D PIC simulation results in both axial-azimuthal and radial-azimuthal simulation planes[6–10,24] are the most complete data to study azimuthal instabilities. In particular, the axial-azimuthal plane allows the study of the development of azimuthal instabilities and their impact on axial electron transport. Therefore in this work, the virtual CTS analysis was applied to the axial-azimuthal PIC benchmark results from Charoy et al.[10]. Although the chosen simulation case is non-self consistent, it was subject to an international benchmark effort and the instabilities involved in the simulation are well characterized making it a

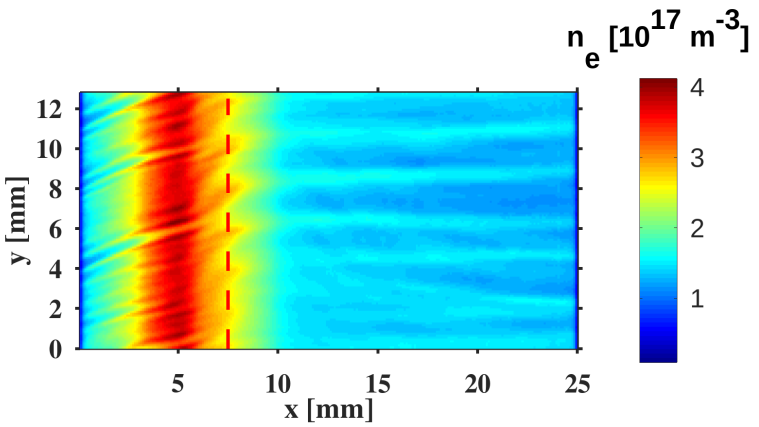

FIG. 2: Typical results from PIC simulations. This snapshot of the electron density is taken at $t = 12.5\,\mu s$. The dashed red line at $x = 7.5\,mm$ indicates the limit between the ionization zone and the acceleration zone which also corresponds to the position of the maximum radial magnetic field and the exit plane of the thruster

solid analysis framework to test the virtual CTS. In the following, a summary of the conditions of the 2D benchmark and key results are presented, but additional details are given in Refs.[10,25]. The 2D simulation domain consists of a 500×256 Cartesian mesh in which the x-axis corresponds to the axial direction while the y-axis corresponds to the azimuthal direction, as illustrated in Fig 1. The curvature of the domain was hence neglected. The axial length L_x was fixed to 25 mm while the azimuthal length L_y was fixed to 12.8 mm. A periodic boundary condition was imposed in the azimuthal direction to circumvent the finite azimuthal length and to reduce the computational time.

Initially, ions and electrons are uniformly distributed over the simulation domain at a density of $5 \times 10^{16} m^{-3}$ and are subject to a 200 V voltage, which was applied between the anode and the cathode. The radial magnetic field profile, as well as the ionization profile, were fixed to remove the low-frequency breathing mode oscillations and highlight the high-frequency instabilities including the ECDI. To maintain the discharge current balance, electrons were injected from the cathode side from an emission line positioned at 1 mm from the right boundary of the simulation domain (Green dashed line in Fig.1), and its potential is adjusted at each step to ensure a zero azimuthally averaged potential at this position[10,25]. This allows keeping a constant averaged po-

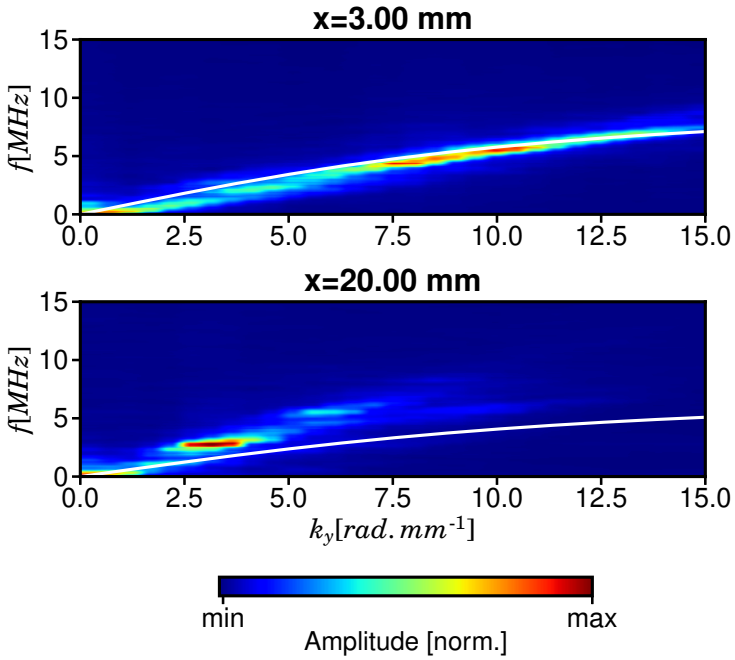

FIG. 3: 2D FFT of the electron density at x = 3 mm and x = 20 mm. Solid white line: ion acoustic dispersion relation.

tential drop between the anode and the emission line. With this method, the right boundary plane has a varying negative potential but this drop in potential between the emission plane and the right boundary plane does not have any useful physical meaning and does not affect the main discharge physics[10,25]. The integration used an explicit scheme with a grid size $\Delta x = 50\,\mu$m and a time step $\Delta t = 5\,$ps. A total of 4×10^6 time steps were simulated resulting in a discharge simulation up to around 20 µs. Nevertheless, due to limited storage capacity, the plasma parameters are only stored every 5000-time steps, thus yielding a sampling time for the electron density of $T_s = 25\,$ns.

A quasi-steady-state was reached at around 12 µs featuring an almost constant discharge current. In Fig 2, a typical 2D map of the electron density at $t = 12.5\,\mu$s is shown. It highlights millimetric fluctuations of the electron density propagating mainly along the azimuthal y-axis. These are marked with a change in the wavelength around the exit plane of the thruster at $x = 7.5\,$mm. In the ionization zone which extends from $x = 2$ to 7.5 mm, the fluctuations have a small wavelength

and their wavevector has both an axial and an azimuthal component. From $x = 7.5$ to 25 mm, which corresponds to the acceleration zone, the structures have a larger wavelength and are almost azimuthal.

A spatial and temporal Fourier analysis of these maps between 16 and 20 µs highlights a continuous dispersion relation in the ionization zone (Iz) that shows a good correspondence with the modified ion-acoustic wave dispersion relation from Lafleur et al.[7,8], as illustrated in Fig 3. The mode corresponding to the maximum growth rate under the ion-acoustic wave approximation is identified at $k_{Iz} \approx 8\,\mathrm{rad.mm^{-1}}$ and has a high frequency $f_{Iz} \approx 5\,\mathrm{MHz}$. In the acceleration zone (Acc), the fit with the modified ion-acoustic dispersion relation is less satisfying. Still, the dynamics is dominated by a single mode at $k_{Acc} \approx 3\,\mathrm{rad.mm^{-1}}$ at a lower frequency $f_{Acc} \approx 3\,\mathrm{MHz}$. The underlying reason for this change in the dynamics is yet not clearly understood and, in the following, we mainly focus on the estimation of the fluctuation rate from the PIC simulation results.

The fluctuation rate from PIC data is assessed by calculating the fluctuation in time and averaging the results azimuthally for each axial position. It is expressed as it follows:

$$\left.\frac{\delta n_e}{n_e}\right|_{PIC}(x) = \left\langle \frac{\sqrt{< n_e^2 >_t - < n_e >_t^2}}{< n_e >_t} \right\rangle_y . \tag{1}$$

The blue curve in Fig 4 shows the axial evolution of the fluctuation rate between 12 µs and 20 µs for the simulated benchmark case. The profile exhibits a large axial variation as already observed by T.Lafleur et al.[8] in the first microseconds of a self-consistent 2D (axial-azimuthal) PIC simulation, that seems to be linked to the ionization profile. Indeed, the fluctuation rate decreases from 10% close to the anode to a minimum of 2.6% at $x = 6.4\,\mathrm{mm}$. This coincides with the maximum ionization rate imposed in the simulation. Then, it increases with small oscillations in the plume to stabilize at around 7% after $x = 20\,\mathrm{mm}$.

In the following, the blue curve will be used as a reference for the comparison with the virtual CTS results.

B. Collective Thomson Scattering Analysis

Collective Thomson scattering describes a scattering phenomenon in which the wavelength of scattering λ is larger or comparable to the Debye length λ_D[26–28]. An incident laser beam at a fixed wave vector $\mathbf{k_i}$ is applied upon the plasma and accelerated electrons behave like dipoles and scatter a part of the incident electromagnetic field at the same wavelength as the incoming field. The

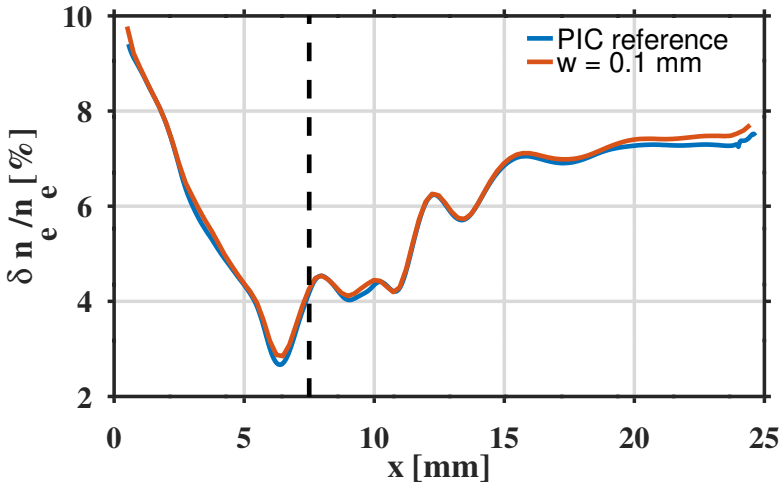

FIG. 4: The axial variation of the electron density fluctuation rate in the simulation case from Charoy et al.[10].The blue curve corresponds to the reference fluctuation rate from PIC results using Eq 1. The red curves corresponds to the synthetical fluctuation rate from the virtual CTS at a waist $w = 0.1\,\text{mm}$ based on Eq 7. Black dashed line at $x = 7.5\,\text{mm}$ corresponds to the position of the maximum radial magnetic field and the exit plane of the thruster.

scattered fields add up to yield the total scattered field. This sum can be constructive or destructive depending on the phase correlation between the electrons' positions. This correlation might occur if coherent structures are propagating through the medium. If so, these can be highlighted by varying the observation length scale of the scattering experiment to match the length scale of the propagating structures. The wave vector $\mathbf{k}$ along which the CTS is performed is called the scattering vector and is determined using Bragg's relation, relating the wave vector $\mathbf{k}$ to the difference between the laser wave vector $\mathbf{k_i}$ and the scattered wave vector $\mathbf{k_s}$, as it follows: $\mathbf{k} = \mathbf{k_s} - \mathbf{k_i}$. Hence, by changing the angle between these vectors, it is possible to change the norm of the scattering wave vector $\mathbf{k}$ and thus to probe the medium at different scales. In practice, the scattering wave vector $\mathbf{k}$ is changed using a translating mirror to vary the angle between $\mathbf{k_s}$ and $\mathbf{k_i}$.

For a fixed $\mathbf{k}$, the resulting signal is proportional to the Fourier transform of the electron density along $\mathbf{k}$ in the scattering volume $\mathscr{V}$ and is recorded as a function of time, such as:

$$s(\mathbf{k},t) = \int_{\mathscr{V}} e^{i\mathbf{k}\cdot\mathbf{r}} n_e(r,t) d^3\mathbf{r}. \tag{2}$$

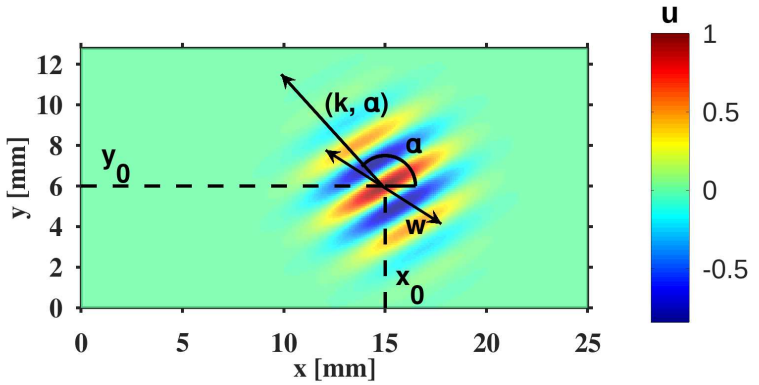

FIG. 5: 2D configuration for the virtual CTS calculation. The scattering volume is a Gaussian profile with a waist $w = 3\,\text{mm}$. The phase factor in the Fourier transform is directed along the scattering vector $\mathbf{k}$, here expressed in polar coordinates with $\alpha = 120°$ and $k = 3\,\text{rad.mm}^{-1}$

Further frequency analysis is usually performed over the total acquisition duration T and provides the spectral density of the scattering signal $S(\mathbf{k},\omega)$. This quantity is proportional to the dynamic form factor and is expressed here as it follows:

$$S(\mathbf{k},\omega) = \left| \int_{\mathscr{V},T} e^{i(\mathbf{k}\cdot\mathbf{r}-\omega t)} n_e(r,t) d^3\mathbf{r} dt \right|^2 . \tag{3}$$

The integral over all frequencies of Eq3 is noted $S(\mathbf{k})$ and is proportional to the static form factor, usually measured in CTS experiments. $S(\mathbf{k})$ is written as:

$$S(\mathbf{k}) = \int_{\omega} S(\mathbf{k},\omega) d\omega. \tag{4}$$

Finally, the total fluctuation of the electron density can be related directly to the static factor, using Parceval's theorem, yielding the following relation:

$$< n_e^2 >= \int_{\mathbf{k}} S(\mathbf{k}) d\mathbf{k}, \tag{5}$$

To perform a virtual CTS on PIC results, we adapt the former integral to a 2D geometry. This is illustrated in Fig 5. The scattering volume V_s, defined as the intersection between the laser beam and the 2D map, is modeled using a Gaussian intensity profile u in polar coordinates with a fixed waist w, such as:

$$u(r) = \frac{1}{\pi w^2} e^{-\frac{r^2}{w^2}}.$$

A 2D local spatial Fourier transform is applied to the electron density maps from the PIC simulation along a fixed scattering vector $\mathbf{k}$ given in polar coordinates (k, α). This enables to probe structures at a given scale k and that are propagating at a given angle α. The virtual scattered field is thus expressed as:

$$S_{PIC}(\mathbf{k}, \mathbf{r_0}, t) = \int_{\mathscr{A}} e^{i\mathbf{k}\cdot(\mathbf{r}-\mathbf{r_0})} u(\mathbf{r}-\mathbf{r_0}) n_e(r,t) d^2\mathbf{r}, \tag{6}$$

where $\mathbf{r_0}$ is the center of the 2D equivalent of the scattering volume $\mathscr{A}$, i.e the center of the Gaussian profile.

The laser intensity profile is applied at each point $r_0 = (x_0, y_0)$ of a rectangular grid at a step $\Delta x_0 = \Delta y_0 = 1\,\text{mm}$. Each position represents a different Thomson scattering experiment where the scattering vector $\mathbf{k} = (k, \alpha)$ is varied by changing both the norm k and angle α. The angle was varied with a resolution of 1° from 0° to 180°, whereas the norm k is varied with a resolution of $0.3\,\text{rad.mm}^{-1}$ from $0.5\,\text{rad.mm}^{-1}$ to $12.5\,\text{rad.mm}^{-1}$. The laser waist is fixed to 3 mm for the reference case as usually used in CTS experiments. Besides, this value offers good analysis features for simulations, considering the size of the structures we want to investigate.

Virtual CTS can be understood as a windowed Fourier transform, for which the chosen window is a 2D Gaussian function, centered at r_0 and which has a standard deviation $\sigma = \frac{w}{\sqrt{2}}$. Similar to windowed Fourier transform, virtual CTS has two main advantages. First, it limits the analysis to an area proportional to the laser beam waist w^2. Second, it introduces a diagnostic length scale $\lambda = \frac{2\pi}{|k|}$ to highlight fluctuations occurring at the same scale as λ. This offers both spatial localization and selectivity over the k-component within the uncertainty inequality limit.

The electron density fluctuation rate is calculated also from the static form factor, using Eq5. However, the calculation yields the root mean square (rms) of the electron density, weighted by the square of the laser intensity profile u^2, denoted as $< n_e^2 u^2 >_{\mathscr{A},T}$. The operator $< . >_{\mathscr{A},T}$ corresponds to the average over the area delimited by the weighting function u^2, such as :

$$< n_e^2 u^2 >_{\mathscr{A},T} = \frac{\int_{\mathscr{A},T} n_e^2 u^2 d^2 r dt}{\int_{\mathscr{A},T} u^2 d^2 r dt}$$

which ensures that $< n_e^2 u^2 >_{\mathscr{A},T}$ is homogeneous to a density.

The u^2 stems from Parceval's theorem since the scattering integral is also the Fourier transform of a Gaussian weighted electron density map. Ergo, the fluctuation rate is expressed as:

$$\left.\frac{\delta n_e}{n_e}\right|_{CTS} = \left\langle \frac{\sqrt{< n_e^2 u^2 >_{\mathscr{A},T} - < n_e u^2 >^2_{\mathscr{A},T}}}{< n_e u^2 >_{\mathscr{A},T}} \right\rangle_y . \tag{7}$$

This definition of the fluctuation rate is consistent with Eq1 for small waists. Indeed as the waist tends to 0, the normalized laser profile converges to the Dirac distribution. Consequently, the axial profile of the weighted electron density in the scattering volume converges also to the reference PIC profile, as it is illustrated in Fig 4 for a waist of $w = 0.1\,\text{mm}$.

C. Pre-Processing of the PIC results

To obtain the results presented in the following sections, PIC results were pre-processed before generating a virtual Thomson scattering signal. The time average was subtracted from the typical 2D map to highlight the fluctuations of the density. This was possible because the benchmark test case reaches a quasi-steady state. Moreover, to reduce the computational cost, the spatial resolution of the PIC simulation was divided by a factor of 2. Namely, the 2D electron density maps were interpolated over a 251×128 grid instead of the initial 501×256 grid. We have checked that the percent error introduced by this interpolation was less than 0.03% on the averaged plasma parameters and the reference fluctuation rate calculated for PIC results with Eq1.

A total of $N = 150$ time-samples were analyzed using this method, resulting in a temporal signal that extends on $3.75\,\mu\text{s}$. In the azimuthal direction y, using the periodic boundary condition, each 2D map of the electron density was extended by a length equal to L_y (Figure 1) to reduce the edge effect in case the waist extends beyond the simulation domain in that direction. Along the axial direction x, the data was not extended when applying the virtual CTS. Then, edge effects close to the axial boundaries will impact virtual CTS results. In the following, for waists of $w = 0.1, 1$ and 3 mm, the comparison of results will be carried out mostly for $3 \leq x \leq 21\,\text{mm}$. The time step of the temporal scattering signal is $\Delta t = 25\,\text{ns}$ which corresponds to a sampling rate of $40\,\text{MHz}$. A complex time-Fourier transform was performed over the sample. The modulus of the spectrum was averaged along the y-direction, to reduce the numerical noise. This was possible since the spectral properties of the azimuthal modes in the benchmark model do not depend on the azimuthal positions.

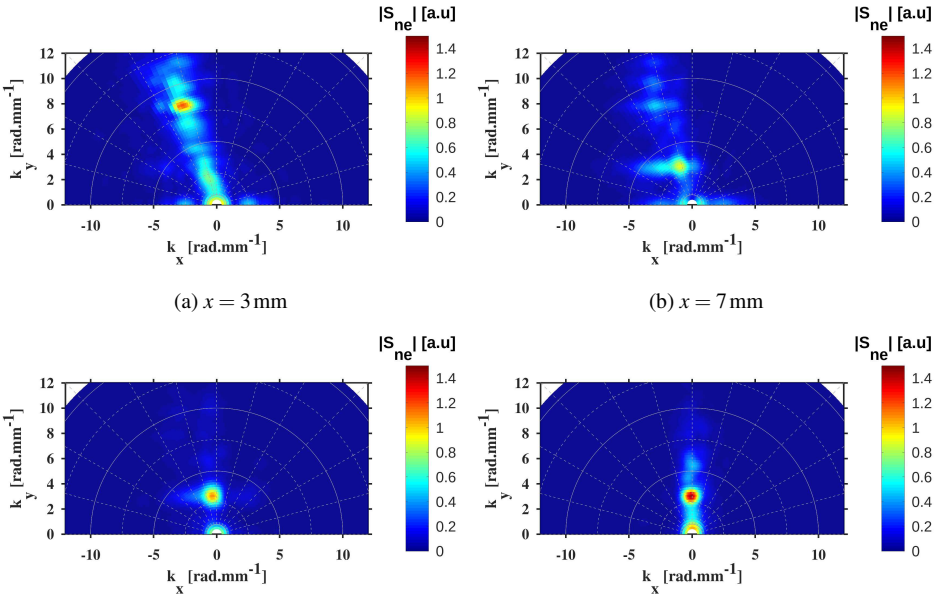

(a) $x = 3\,\mathrm{mm}$ (b) $x = 7\,\mathrm{mm}$

(c) $x = 10\,\mathrm{mm}$ (d) $x = 20\,\mathrm{mm}$

FIG. 6: 2D polar maps of the intensity of the scattering signal at different axial positions

III. RESULTS

A. Amplitude variation of the dominant modes

First, we examine the virtual CTS result at a fixed time t to identify the dominant structures present in the discharge.

Fig 6 shows the variation of the scattering signal along the wave vector k_x and k_y at different axial position, at $t = 12.5\,\mu\mathrm{s}$, when the simulation has reached a quasi-steady state, for $|\mathbf{k}|$ between $0.5\,\mathrm{rad.mm^{-1}}$ and $12.5\,\mathrm{rad.mm^{-1}}$. Fig 6a reports a snapshot of the 2D polar map of the scattering signal at $x = 3\,\mathrm{mm}$ and shows multiple modes propagating inward, to the anode, at an angle of 110°. First, there is an intense and highly peaked mode at $k_y = 8\,\mathrm{rad.mm^{-1}}$ that is identified as the ion-acoustic wave based on the plasma parameters from the PIC simulation. Then, there is a less intense but broad mode at around $k_y \approx 3\,\mathrm{rad.mm^{-1}}$ These two modes (at $k_y = 8\,\mathrm{rad.mm^{-1}}$ and $k_y = 3\,\mathrm{rad.mm^{-1}}$) correspond to the dominant coherent structures propagating in the thruster's channel

and in the following, we will focus on their axial variation. Downstream in the ionization zone, at $x = 7\,\text{mm}$, the intensity of the $k_y = 8\,\text{rad.mm}^{-1}$ mode weakens favouring the second mode at $k_y = 3\,\text{rad.mm}^{-1}$ which becomes dominant as shown in Fig 6b. In the acceleration zone, at $x = 10$ and 20 mm, (Fig 6c and 6d), the $3\,\text{rad.mm}^{-1}$ mode increases in intensity and its direction shifts slowly from 110° to 90°. The change of direction occurs mainly at the beginning of the acceleration zone where the ion velocity increases greatly. This is consistent with previous observations in Honoré *et al.*[20] suggesting that the modes are convected with ions as they are accelerated. The inward negative component k_x, in the ionization zone, is cancelled to an almost zero value, in the observation frame of reference, as the positive outward velocity component of the ions begins to increase in the acceleration zone.

Moreover, this change of direction concurs with a change in the intensity of the modes. This is illustrated in Fig 7 which shows the intensity evolution of the two dominant modes as a function of the axial position x. In addition to the previous observations, the intensity of the $3\,\text{rad.mm}^{-1}$ mode increases linearly along the thruster axis. The change in the direction of the modes happens at a constant k_y while the magnitude of the k_x component slowly decreases to 0. The decrease of the intensity at $x = 21\,\text{mm}$ is due to the edge effects near the simulation boundaries and the local extremum at $x = 3\,\text{mm}$ is mainly due to the presence of multiple small peaks at small k that are difficult to resolve. The mode at $8\,\text{rad.mm}^{-1}$ demonstrates also similar dynamics concerning the wave vector variation. Its decrease at the beginning of the acceleration zone is however very sharp and the k_x component blue converges quickly to 0, contrasting with the smooth behavior of the small k modes.

B. Dispersion Relation

In the previous section, two coherent modes at $k_y = 8\,\text{rad.mm}^{-1}$ and $k_y = 3\,\text{rad.mm}^{-1}$ were identified in the simulation. To determine the frequencies of these modes, a spectral analysis of the time-dependent scattered signal is performed in the following paragraph.

Fig 8 shows the normalised Fourier transform of the time-dependent scattered signal in the ionization zone, at $x = 3\,\text{mm}$ and at an angle $\alpha = 110°$ and in the acceleration zone, at $x = 20\,\text{mm}$ and at an angle $\alpha = 90°$. The spectra illustrate one well-defined peaks in each case for both modes.

Fig 8a shows that for the $k_y = 3\,\text{rad.mm}^{-1}$ the frequency is different with respect to the observation zone. The mode's mean frequency increases from 1 MHz in the ionization zone to 3 MHz

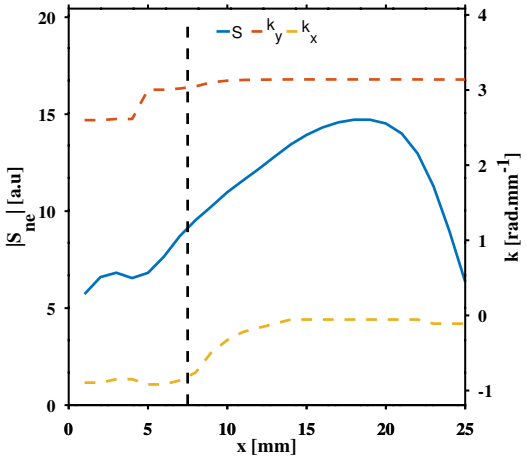

(a) $k = 3\,\mathrm{rad.mm}^{-1}$

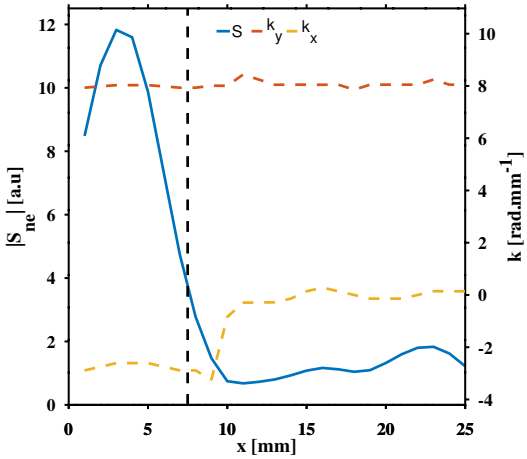

(b) $k = 8\,\mathrm{rad.mm}^{-1}$

FIG. 7: Variation of the dominant modes along the axial direction. The blue curves show the intensity of the scattering signal while, on the secondary axis, the dashed curves show the variation of the axial component k_x and the azimuthal component k_y. The dashed black curve indicates the thruster exit plane and the position of the maximum radial magnetic field.

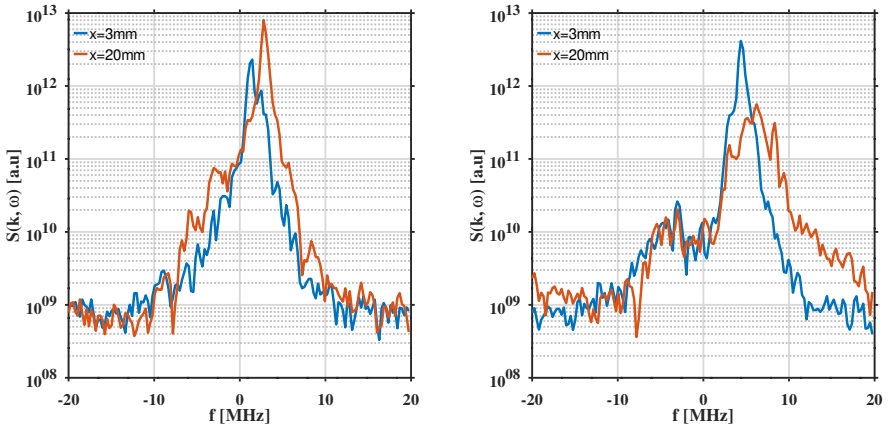

(a) Dynamic form factor for $k_y = 3\,\text{rad.mm}^{-1}$

(b) Dynamic form factor for $k_y = 8\,\text{rad.mm}^{-1}$

FIG. 8: Dynamic form factor for $k_y = 3\,\text{rad.mm}^{-1}$ and $k_y = 8\,\text{rad.mm}^{-1}$ at x =3 mm and 20 mm. Blue curves correspond to $x = 3\,\text{mm}$ and an angle $\alpha = 110°$ and the red curve correspond to $x = 20\,\text{mm}$ and an angle $\alpha = 90°$

in the acceleration zone. The results for the mode at $k_y = 8\,\text{rad.mm}^{-1}$ are presented in Fig 8b. The mode's mean frequency also increases from 4.5 MHz in the ionization zone to 6.5 MHz in the acceleration zone. We also observe a broad peak at a negative frequency that suggests a wave back-flow, however, this would need further investigation.

The dispersion relation, from the virtual Thomson scattering experiment is computed for different observation angles α and at different axial positions. The results show a linear progression of the frequency with respect to the wave number for all the tested angles. The maximum signal is obtained, though, when the angle of the observation is along the main propagation direction i.e $\alpha = 110°$ in the ionization zone and $\alpha = 90°$ in the acceleration zone. Fig 9a and Fig 9b show the respective dispersion relations along these privileged observation angles at $x = 3\,\text{mm}$ and $x = 20\,\text{mm}$ respectively. Two phase velocities are identified using a linear fit, $v_{g,Iz} = 3.5\,\text{km.s}^{-1}$ and $v_{g,Acc} = 6.6\,\text{km.s}^{-1}$. These values are of the same order of magnitude as the measured phase velocities from CTS experiments[13,17], that were conducted on a similar range of wave vectors.

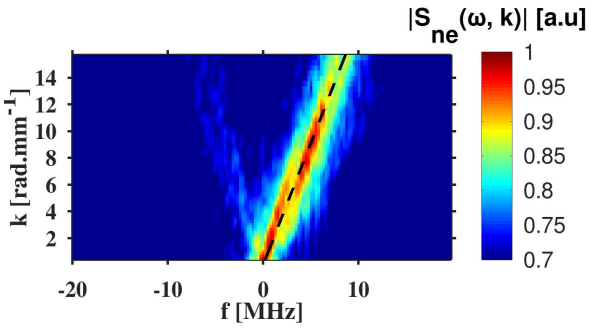

(a) $x = 3$ mm with $\alpha = 110°$

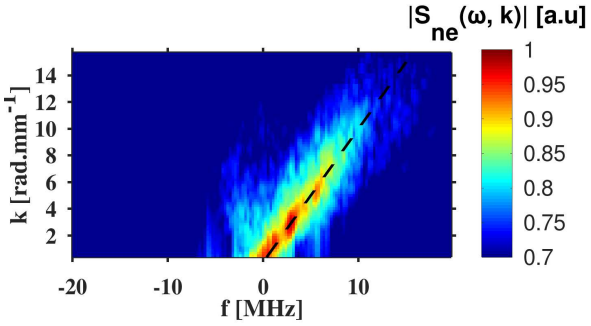

(b) $x = 20$ mm with $\alpha = 90°$

FIG. 9: Dispersion relations derived from the virtual Thomson scattering experiment along the privileged observation angle relative to each zone: (a) corresponds to the ionization zone with $\alpha = 110°$ while (b) corresponds to the acceleration zone with $\alpha = 90°$. The dashed black lines correspond to the best linear fit

C. Electron Density Fluctuation rate

In this section, we derive the electron density fluctuation rate using the virtual CTS for different values of the waist w of the laser beam. The results are then compared with the reference PIC values. In Eq7, the waist appears when we calculate both the mean electron density and its rms since these values are averaged over the scattering volume.

At first, we examine the mean electron density profile. Fig 10 shows the axial profile of the electron density for two different values of the laser waist: $w = 1$ and 3 mm. The laser-beam

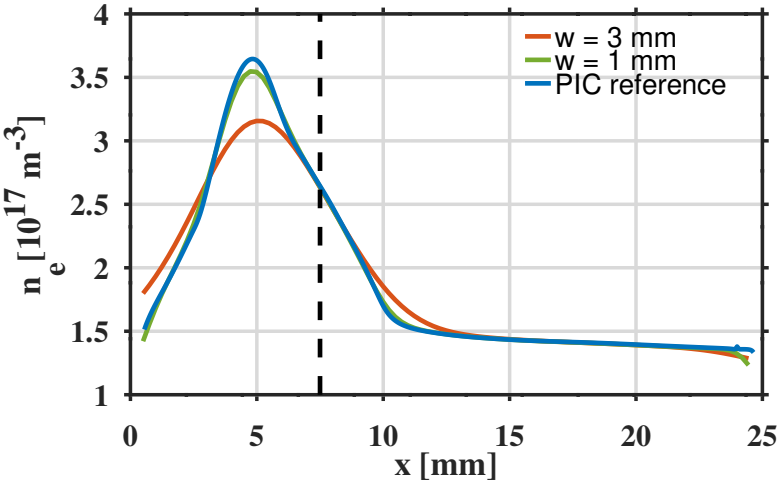

FIG. 10: Axial profile of the electron density for different values of the laser waist: $w = 1$ and 3 mm in the CTS analysis and from the PIC simulations.

weighed electron density maps were averaged over 3.75 µs and the azimuthal direction. The profiles diverge significantly for axial distances between $x = 3$ mm and $x = 10$ mm, where a steep density gradient is observed. This is most noteworthy for a $w = 3$ mm waist with a maximum 11% deviation from the PIC profile at around $x = 5$ mm. For a $w = 1$ mm waist, on the other hand, the deviation is estimated to be a mere 2%. These observations are mainly due to the presence of gradients in the electron density profile inside the scattering volume. Indeed, if the scattering volume has a sufficient spatial extension, the laser profile behaves like a Gaussian filter and smoothens the electron density profile. Depending on how the electrons are distributed in the scattering volume, the locally-averaged electron density is either underestimated or overestimated at a given axial position. In the acceleration zone, between $x = 10$ mm and $x = 214$ mm, where the axial evolution of the electron density is much smoother, the virtual CTS analysis gives results close to the reference PIC profile for $w = 1$ mm and $w = 3$ mm.

Then, we examine the electron density fluctuation rate as introduced in Eq7 for two different values of the laser waist: $w = 1$ and 3 mm and compare it to the PIC reference value. The results are reported on Fig 11. As mentioned in Section II C, we limit our analysis to $3 \leq x \leq 21$ mm. Between $x = 3$ mm and $x = 10$ mm, the virtual CTS estimates an average fluctuation rate at around

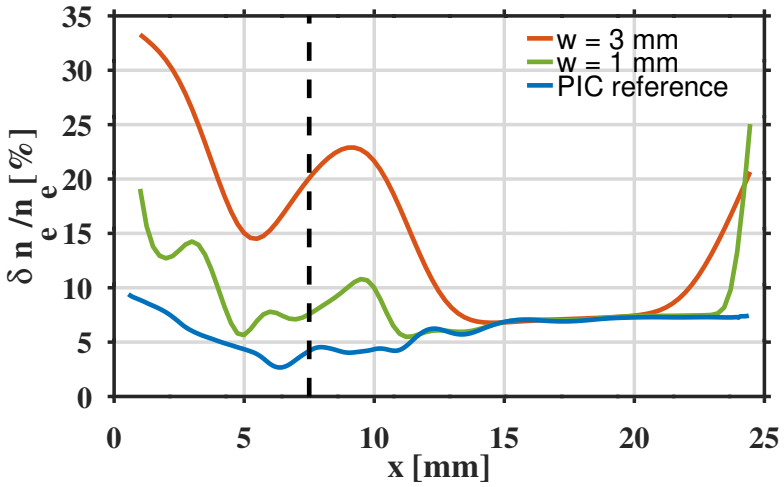

FIG. 11: Axial profile of the electron fluctuation rate for different values of the laser waist: $w = 1$ and 3 mm in the CTS analysis and from the PIC simulations.

20% for $w = 3$ mm, 3 times higher than what the reference PIC profile yields. In contrast, in the acceleration zone, between $x = 10$ mm and $x = 24$ mm, where the axial electron density is almost constant, the virtual CTS for $w = 1$ and 3 mm gives results coherent with the 7% fluctuation rate of the reference PIC profile. The aforementioned smoothing effect of the axially-averaged-electron density profile could not explain alone this difference. Indeed a factor of 2 is also observed for $w = 1$ mm for which the difference in the mean electron density profiles is estimated to be only 2%.

In this regard, the difference, observed in Fig 11 stems then from the numerator of Eq7. This term corresponds, in the framework of CTS, to the integral of the form factor over all possible fluctuations in the scattering volume. Since the volume (Fig 5) has a spatial extension both in the azimuthal and the axial direction, the integrated profiles of the fluctuation rate take into account not only azimuthal fluctuations associated with the propagating modes but also the axial density standard deviation associated with the density gradient. This results in a relatively high value compared to the PIC reference value.

These observations favor the use of smaller waists in CTS experiments for positions where gradients are high to reduce the impact of the waist on the measurement of the density fluctuation

rate. However, this is more challenging in CTS experiments since a smaller w would lead to a degraded k resolution.

IV. CONCLUSION

In this work, 2D axial-azimuthal PIC simulations were analyzed using a virtual CTS. It has been shown that compared to the non-windowed Fourier transform, virtual CTS offers a localized and directional tool to analyze PIC data. The analysis of PIC results using a virtual CTS diagnostic allowed an enhanced characterization of the modes present in the stationary state of a 2D axial-azimuthal PIC simulation[10], not only in the plume but also in the thruster channel. It permitted to resolve two modes at $3\,\mathrm{rad.mm^{-1}}$ and $8\,\mathrm{rad.mm^{-1}}$ propagating all along the thruster axis. Their direction is slightly oblique near the anode and becomes almost azimuthal at the thruster exit plane as they are convected by ions. The observation shows also that when the ions' convection becomes very large, the change in direction concurs with a change in the amplitudes of the modes. The amplitude of the $3\,\mathrm{rad.mm^{-1}}$ mode grows linearly in the acceleration zone while the $8\,\mathrm{rad.mm^{-1}}$ is sharply damped. The dispersion relations (f,k) have been computed using this approach inside the ionization zone in the thruster channel and the acceleration zone and are consistent with the observations in CTS experiments.

On the other hand, the examination of the electron density fluctuation rate shows a strong dependence on the axial position x. Far in the thruster plume, the fluctuation rate is almost constant, while in the ionization zone inside the thruster and near the exit plane, the profile exhibits strong variations. Moreover, the results are shown to strongly depend on the value of the laser beam waist (1 and 3 mm in this work). The study first highlights the importance of an accurate measure of the electron density inside the scattering volume. Since the electron density appears as a dividing factor, a gross estimation can lead to a large difference in the order of magnitude of the fluctuation rate. Recent measurements using incoherent Thomson scattering to estimate the electron density[21] also suggest a similar conclusion. The observations also highlight the impact of the waist on the evaluation of the electron density root-mean-square. Because of its spatial extension, the diagnostic integrates both axial and azimuthal fluctuations. This leads to a different estimation of the fluctuation rate especially in areas with a strong electron density gradient.

Finally, this work has allowed us to clarify further the discrepancies between PIC simulations and CTS experiments on the value of the electron density fluctuation rate. It also underlines the

interest to perform virtual plasma diagnostics on either PIC or fluid simulations since they allow to relate simulations and experiments and foster common ground for comparison and discussion. In this work, the CTS diagnostic was applied to a simplified 2D (axial-azimuthal) test case with a stationary state. In future work, the virtual CTS will be used to analyze a self-consistent time-dependent 2D (axial-azimuthal) simulation closer to the real operation conditions of Hall effect thrusters.

ACKNOWLEDGMENTS

This work has been partially funded by ANR (No. ANR-16-CHIN-003–01) and Safran Aircraft Engines within the project POSEIDON.

DATA AVAILABILITY STATEMENT

The data that support the findings of this study are available from the corresponding author upon reasonable request.

REFERENCES

[1]A. I. Morozov and V. V. Savelyev, "Fundamentals of stationary plasma thruster theory," in *Reviews of Plasma Physics*, edited by B. B. Kadomtsev and V. D. Shafranov (Springer US, Boston, MA, 2000) pp. 203–391.

[2]D. O'Reilly, G. Herdrich, and D. F. Kavanagh, "Electric propulsion methods for small satellites: A review," Aerospace **8** (2021), 10.3390/aerospace8010022.

[3]F. Taccogna, S. Longo, M. Capitelli, and R. Schneider, "Anomalous transport induced by sheath instability in hall effect thrusters," Applied Physics Letters **94**, 251502 (2009), https://doi.org/10.1063/1.3152270.

[4]Y. Raitses, I. D. Kaganovich, A. Khrabrov, D. Sydorenko, N. J. Fisch, and A. Smolyakov, "Effect of secondary electron emission on electron cross-field current in $\mathbf{E} \times \mathbf{B}$ discharges," IEEE Transactions on Plasma Science **39**, 995–1006 (2011).

[5]W. Frias, A. I. Smolyakov, I. D. Kaganovich, and Y. Raitses, "Long wavelength gradient drift instability in hall plasma devices. i. fluid theory," Physics of Plasmas **19**, 072112 (2012), https://doi.org/10.1063/1.4736997.

[6]J. C. Adam, A. Héron, and G. Laval, "Study of stationary plasma thrusters using two-dimensional fully kinetic simulations," Physics of Plasmas **11**, 295–305 (2004), https://doi.org/10.1063/1.1632904.

[7]T. Lafleur, S. D. Baalrud, and P. Chabert, "Characteristics and transport effects of the electron drift instability in hall-effect thrusters," Plasma Sources Science and Technology **26**, 024008 (2017).

[8]T. Lafleur, R. Martorelli, P. Chabert, and A. Bourdon, "Anomalous electron transport in hall-effect thrusters: Comparison between quasi-linear kinetic theory and particle-in-cell simulations," Physics of Plasmas **25**, 061202 (2018), https://doi.org/10.1063/1.5017626.

[9]K. Hara, "An overview of discharge plasma modeling for hall effect thrusters," Plasma Sources Science and Technology **28**, 044001 (2019).

[10]T. Charoy, J. P. Boeuf, A. Bourdon, J. A. Carlsson, P. Chabert, B. Cuenot, D. Eremin, L. Garrigues, K. Hara, I. D. Kaganovich, A. T. Powis, A. Smolyakov, D. Sydorenko, A. Tavant, O. Vermorel, and W. Villafana, "2D axial-azimuthal particle-in-cell benchmark for low-temperature partially magnetized plasmas," Plasma Sources Science and Technology **28**, 105010 (2019).

[11]A. Lazurenko, V. Vial, M. Prioul, and A. Bouchoule, "Experimental investigation of high-frequency drifting perturbations in hall thrusters," Physics of Plasmas **12**, 013501–013501–9 (2005), https://doi.org/10.1063/1.1818698.

[12]A. Lazurenko, T. D. de Wit, C. Cavoit, V. Krasnoselskikh, A. Bouchoule, and M. Dudeck, "Determination of the electron anomalous mobility through measurements of turbulent magnetic field in hall thrusters," Physics of Plasmas **14**, 033504 (2007), https://doi.org/10.1063/1.2535813.

[13]S. Tsikata, N. Lemoine, V. Pisarev, and D. M. Grésillon, "Dispersion relations of electron density fluctuations in a hall thruster plasma, observed by collective light scattering," Physics of Plasmas **16**, 033506 (2009), https://doi.org/10.1063/1.3093261.

[14]J. Cavalier, N. Lemoine, G. Bonhomme, S. Tsikata, C. Honoré, and D. Grésillon, "Hall thruster plasma fluctuations identified as the $\mathbf{E} \times \mathbf{B}$ electron drift instability: Modeling and fitting on experimental data," Physics of Plasmas **20**, 082107 (2013), https://doi.org/10.1063/1.4817743.

[15]Z. A. Brown and B. A. Jorns, "Spatial evolution of small wavelength fluctuations in a hall thruster," Physics of Plasmas **26**, 113504 (2019), https://doi.org/10.1063/1.5116708.

[16]I. D. Kaganovich, A. Smolyakov, Y. Raitses, E. Ahedo, I. G. Mikellides, B. Jorns, F. Taccogna, R. Gueroult, S. Tsikata, A. Bourdon, J.-P. Boeuf, M. Keidar, A. T. Powis, M. Merino,

M. Cappelli, K. Hara, J. A. Carlsson, N. J. Fisch, P. Chabert, I. Schweigert, T. Lafleur, K. Matyash, A. V. Khrabrov, R. W. Boswell, and A. Fruchtman, "Physics of eb discharges relevant to plasma propulsion and similar technologies," Physics of Plasmas **27**, 120601 (2020), https://doi.org/10.1063/5.0010135.

[17]S. Tsikata, C. Honoré, N. Lemoine, and D. M. Grésillon, "Three-dimensional structure of electron density fluctuations in the hall thruster plasma: $\mathbf{E}\times\mathbf{B}$ mode," Physics of Plasmas **17**, 112110 (2010), https://doi.org/10.1063/1.3499350.

[18]S. Tsikata, C. Honoré, and D. Grésillon, "Collective thomson scattering for studying plasma instabilities in electric thrusters," Journal of Instrumentation **8**, C10012–C10012 (2013).

[19]S. Tsikata, J. Cavalier, A. Héron, C. Honoré, N. Lemoine, D. Grésillon, and D. Coulette, "An axially propagating two-stream instability in the hall thruster plasma," Physics of Plasmas **21**, 072116 (2014), https://doi.org/10.1063/1.4890025.

[20]C. Honoré, S. Tsikata, D. Grésillon, A. Héron, N. Lemoine, and J. Cavalier, "Hall thruster small scale plasma fluctuations: Qualifying 2D pic simulations against collective scattering experimental data," (The 32nd Int. Electric Propulsion Conf.11/9-5/9/2011, Wiesbaden).

[21]S. Tsikata, A. Héron, and C. Honoré, "Hall thruster microturbulence under conditions of modified electron wall emission," Physics of Plasmas **24**, 053519 (2017), https://doi.org/10.1063/1.4984255.

[22]S. Tsikata and K. Hara, "Plasma instabilities in cross-field configuration: an analysis of the relevance of different modes for electron transport," (the 36th International Electric Propulsion Conference, Vienna, Austria, September 2019).

[23]A. T. Powis and M. N. Shneider, "Particle-in-cell modeling of laser thomson scattering in low-density plasmas at elevated laser intensities," Physics of Plasmas **25**, 053513 (2018), https://doi.org/10.1063/1.5029820.

[24]J.-P. Boeuf, "Tutorial: Physics and modeling of hall thrusters," Journal of Applied Physics **121**, 011101 (2017), https://doi.org/10.1063/1.4972269.

[25]J. P. Boeuf and L. Garrigues, "E × B electron drift instability in hall thrusters: Particle-in-cell simulations vs. theory," Physics of Plasmas **25**, 061204 (2018), https://doi.org/10.1063/1.5017033.

[26]E. Holzhauer and J. H. Massig, "An analysis of optical mixing in plasma scattering experiments," Plasma Physics **20**, 867–877 (1978).

[27]D. H. Froula, S. H. Glenzer, N. C. Luhmann, and J. Sheffield, "Chapter 2 and chapter 5," in *Plasma Scattering of Electromagnetic Radiation (Second Edition)* (Academic Press, Boston, 2011) second edition ed., pp. 103–142.

[28]v. d. Meiden, H.J., *Thomson scattering on low and high temperature plasmas*, Phd Thesis 1 (Research TU/e / Graduation TU/e), Technische Universiteit Eindhoven, Eindhoven (2011), iSBN: 9789038624242.

PLEASE CITE THIS ARTICLE AS DOI: 10.1063/5.0073215

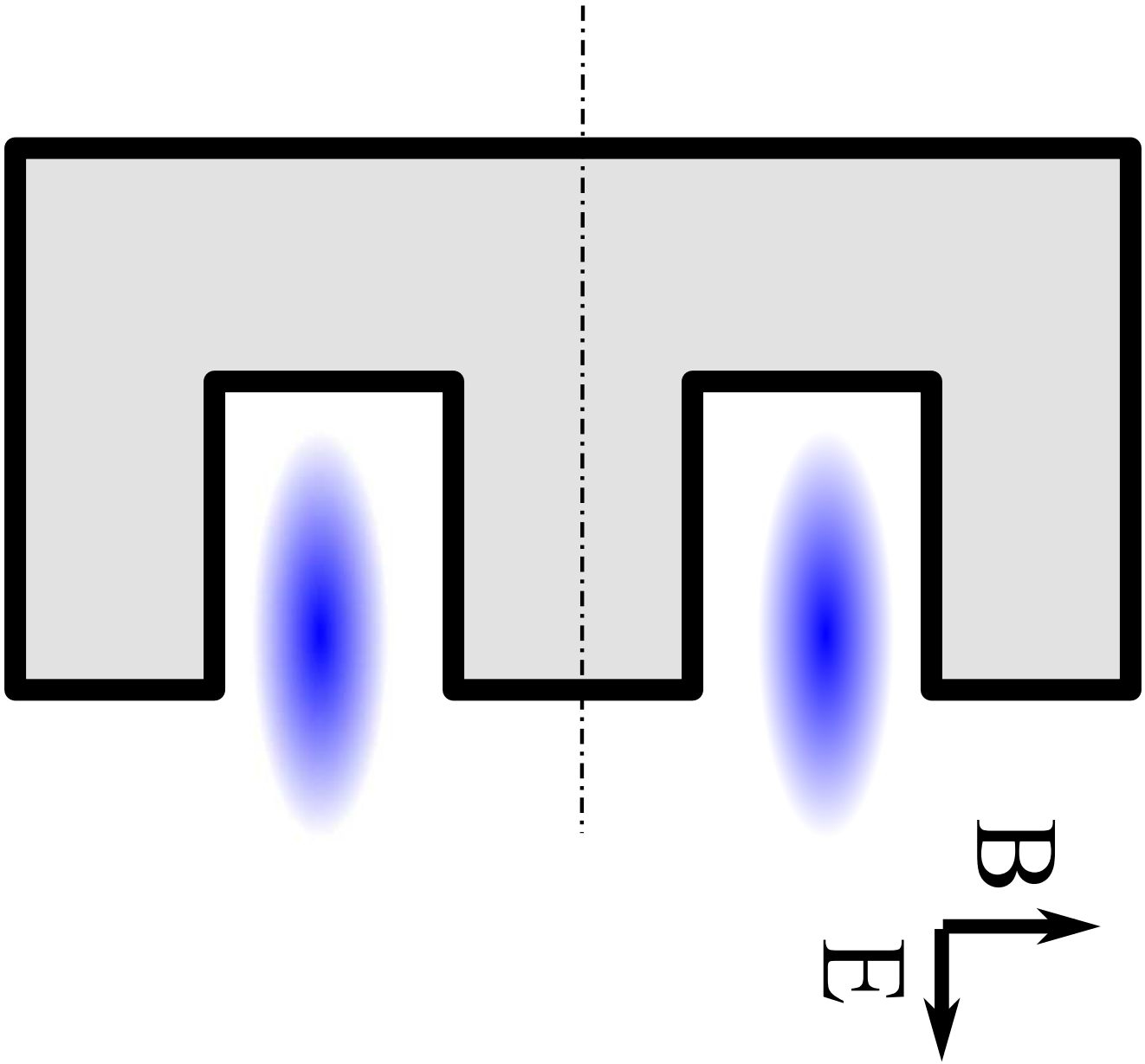

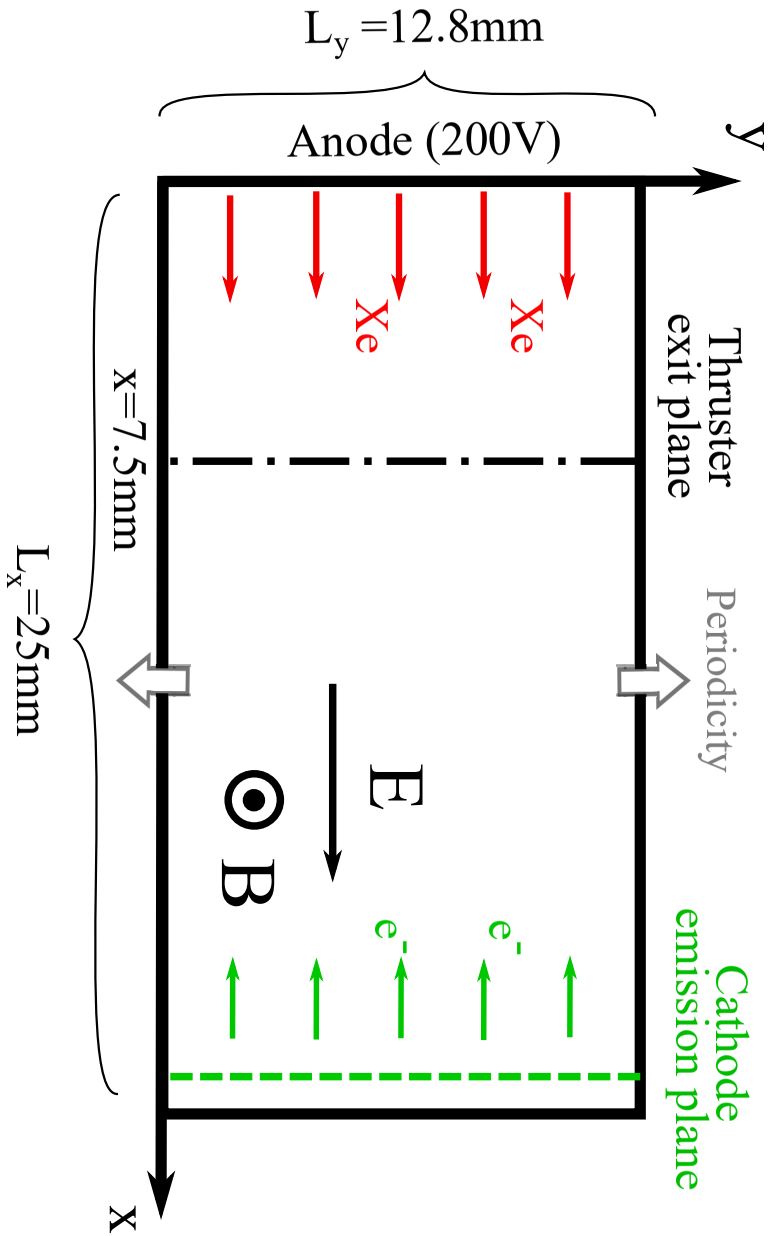

PLEASE CITE THIS ARTICLE AS DOI: 10.1063/5.0073215

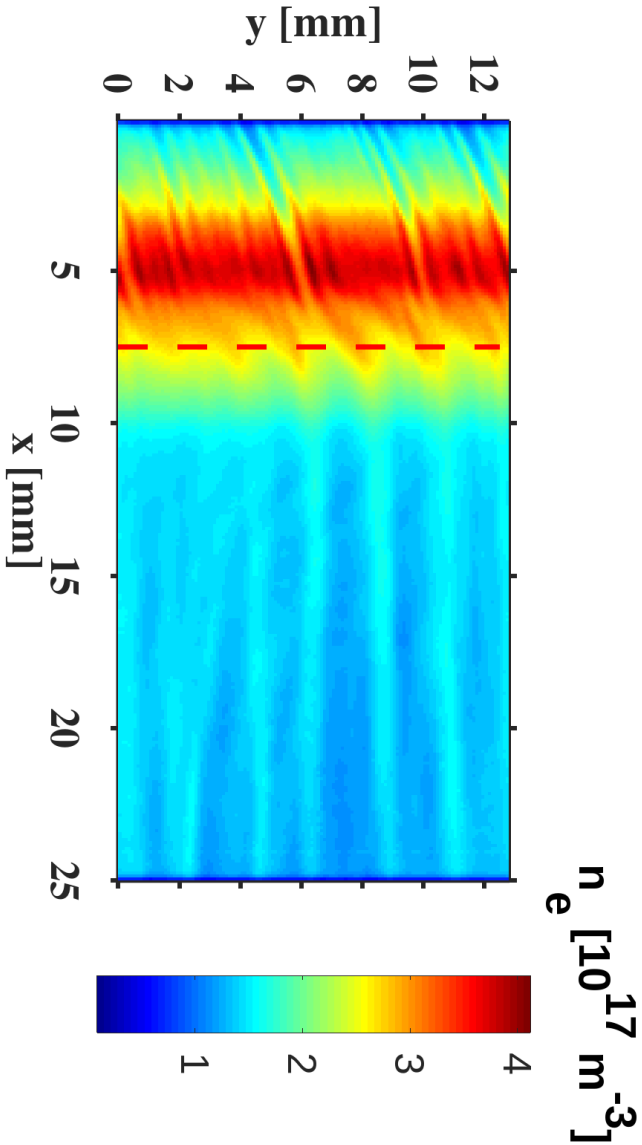

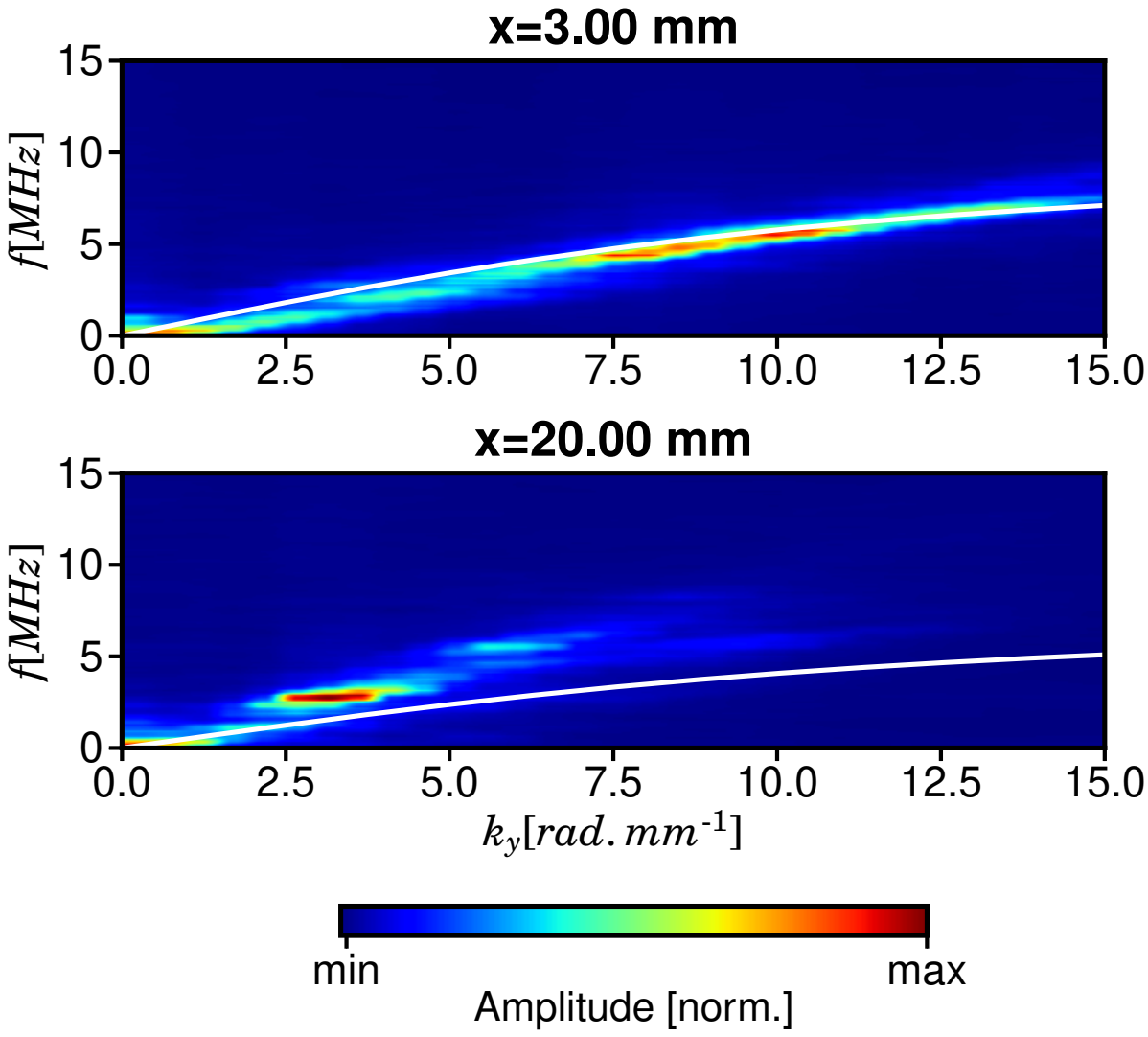

PLEASE CITE THIS ARTICLE AS DOI: 10.1063/5.0073215

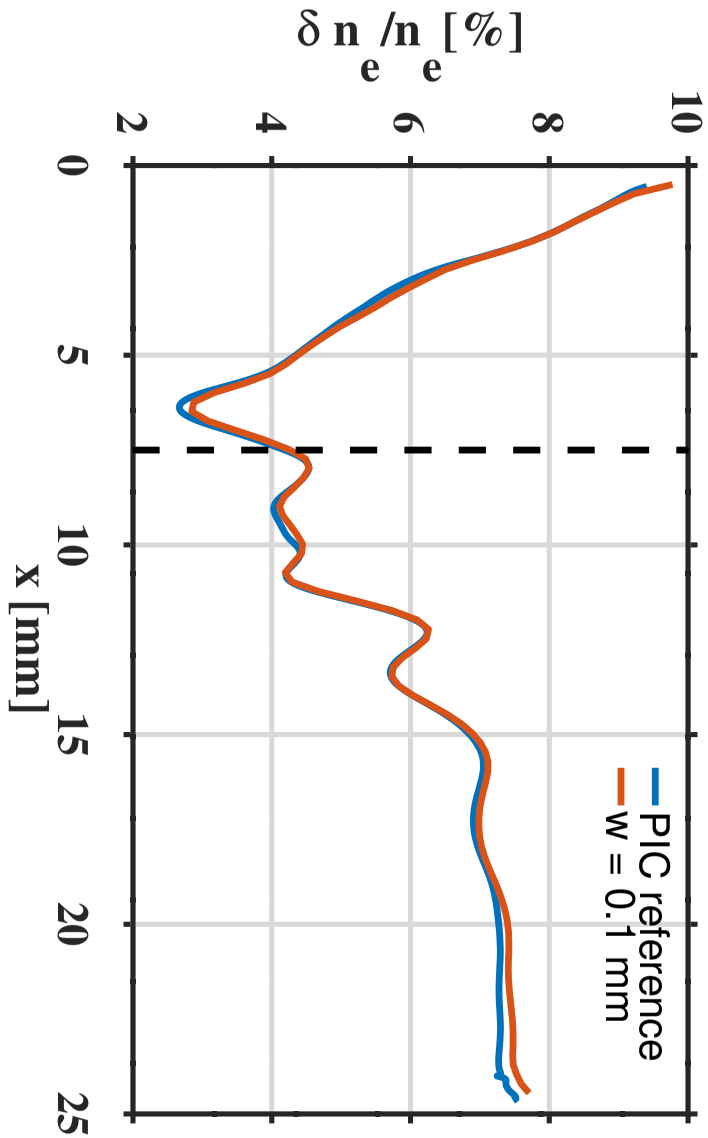

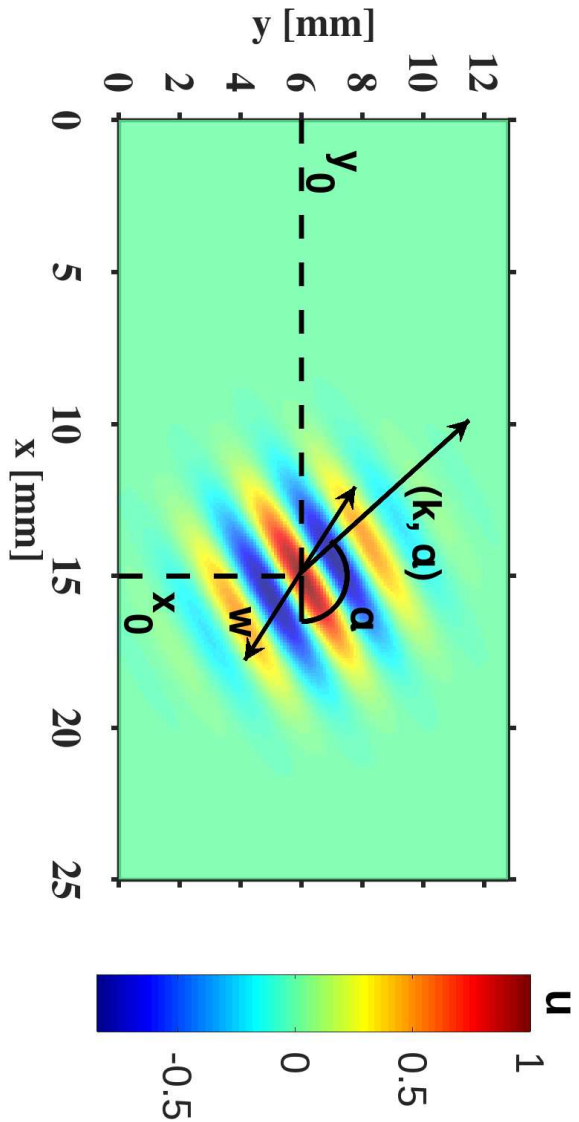

PLEASE CITE THIS ARTICLE AS DOI: 10.1063/5.0073215

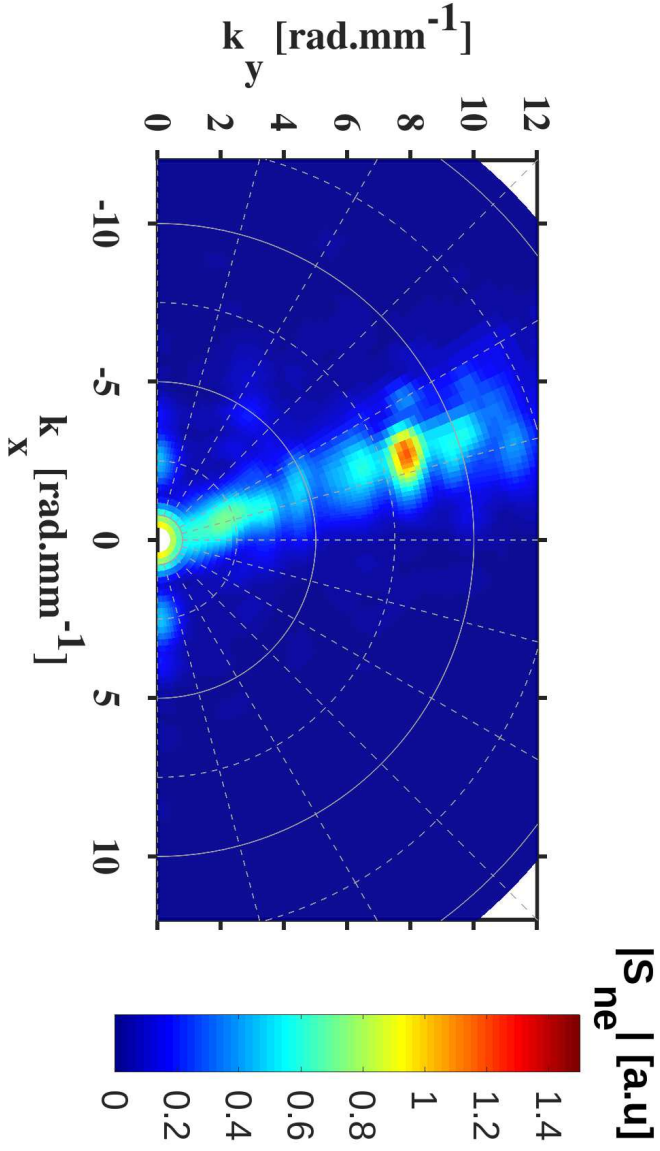

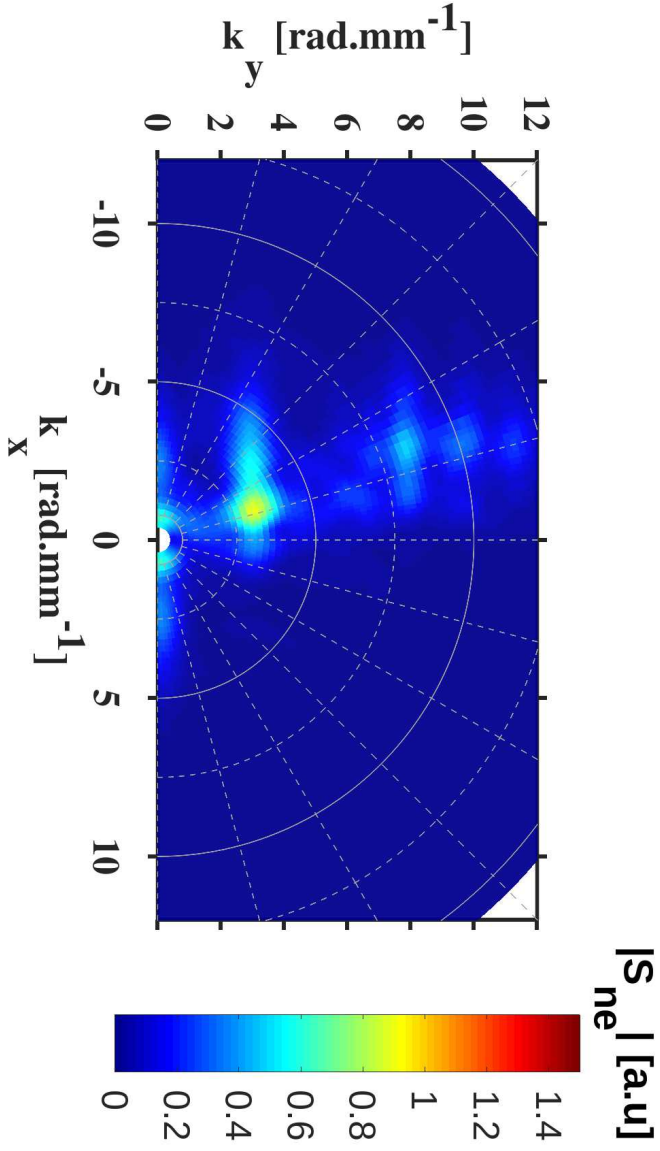

PLEASE CITE THIS ARTICLE AS DOI: 10.1063/5.0073215

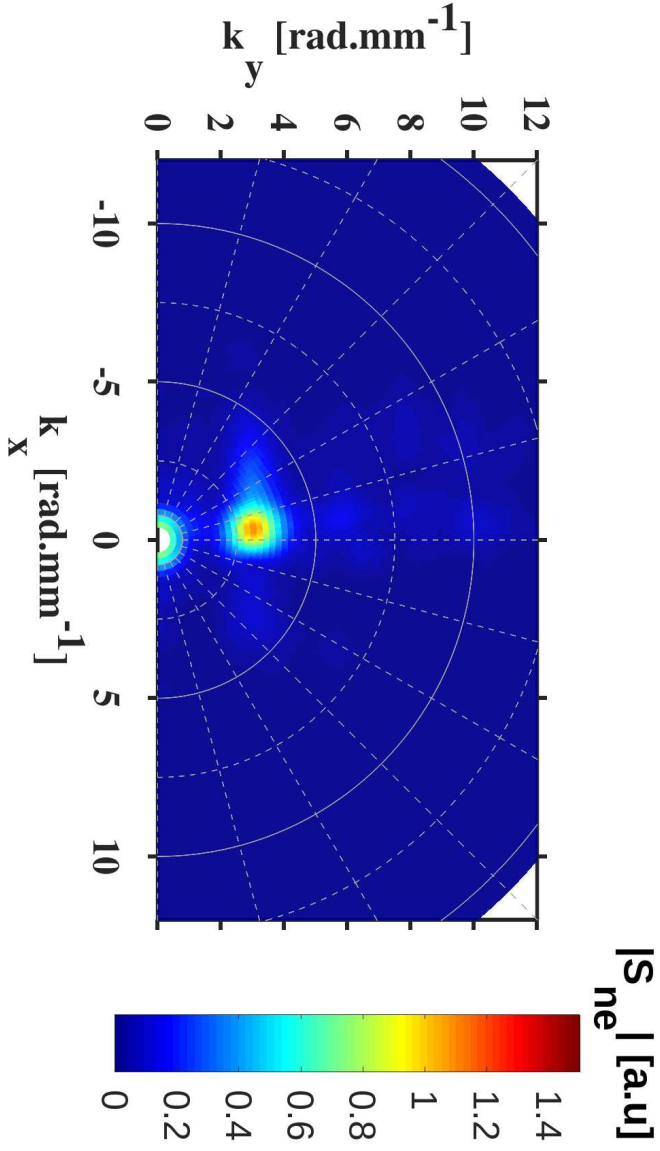

PLEASE CITE THIS ARTICLE AS DOI: 10.1063/5.0073215

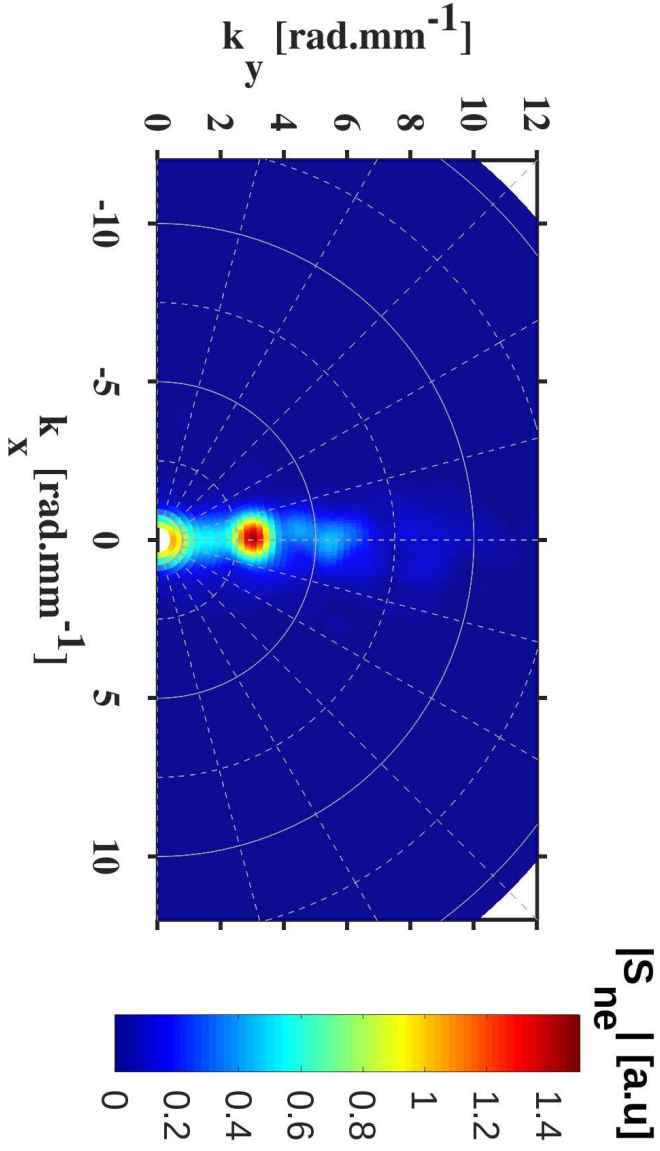

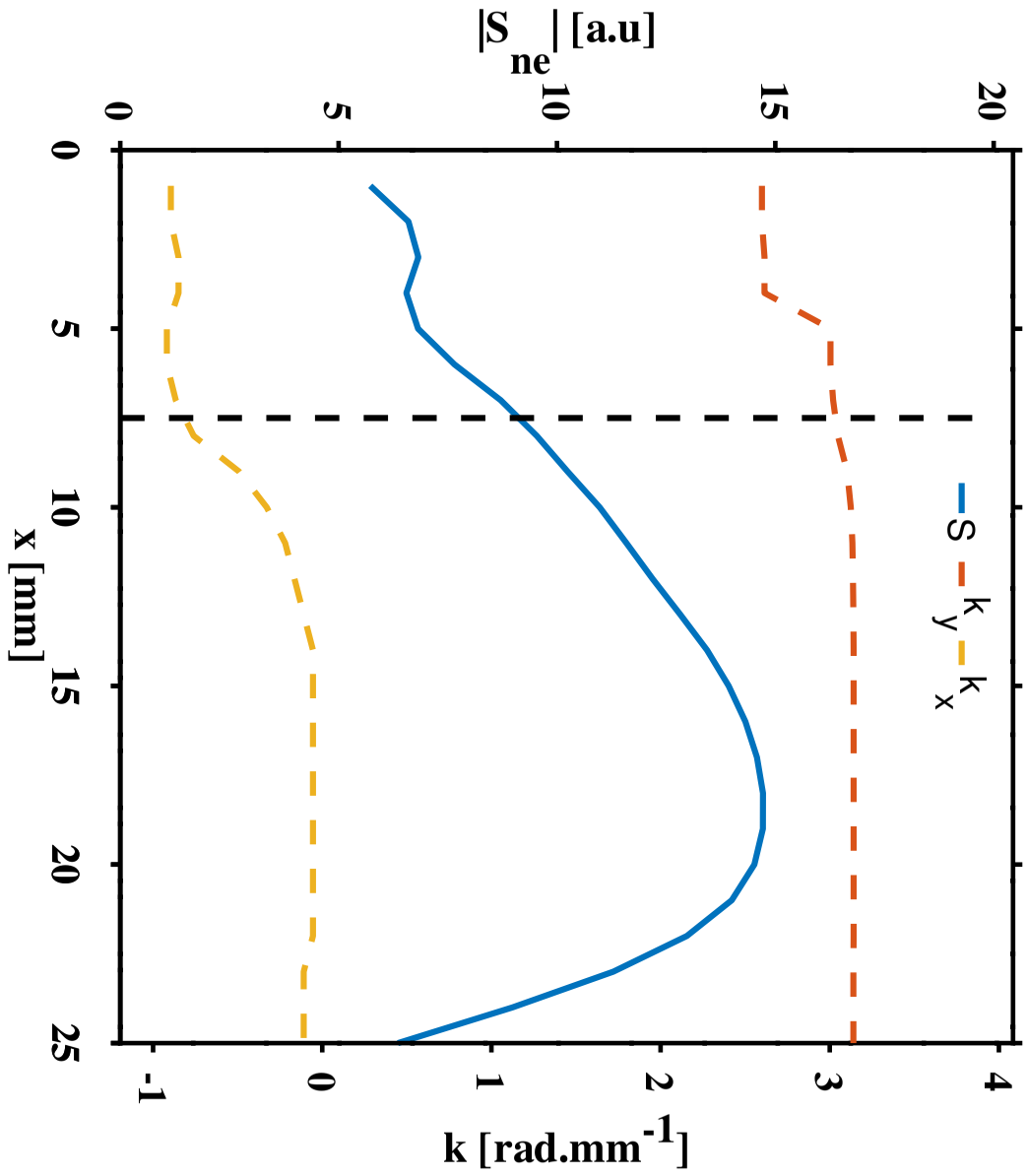

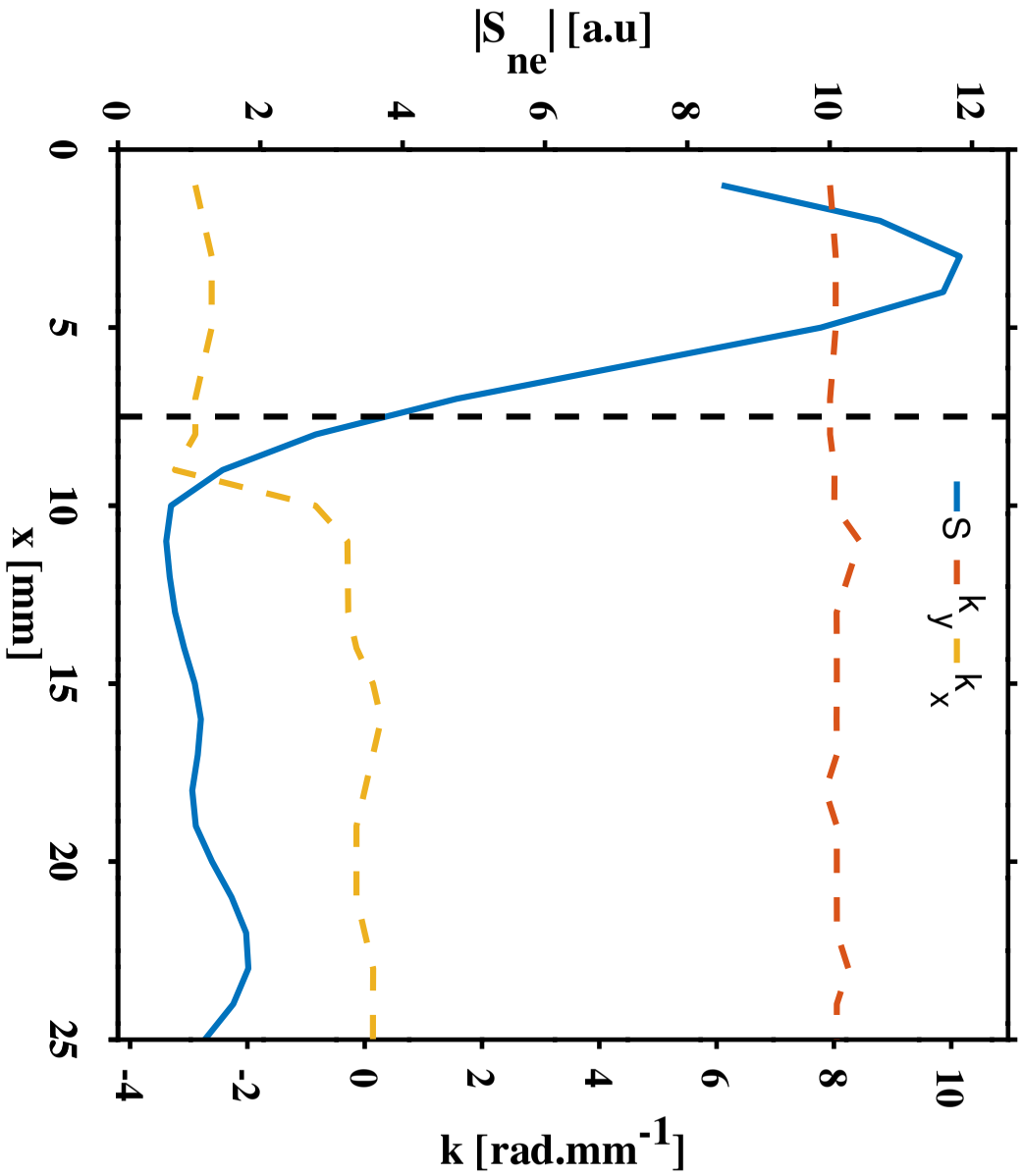

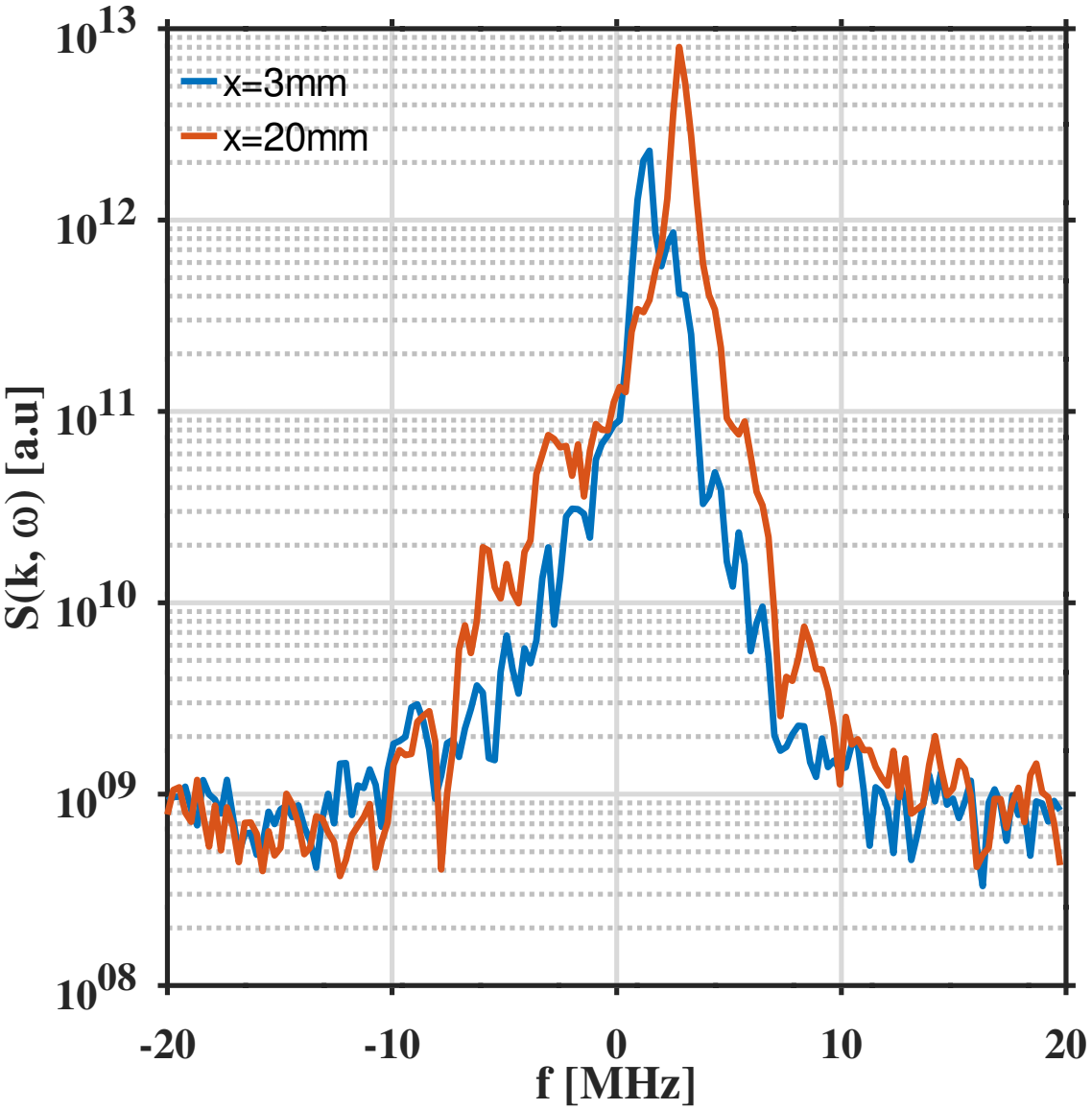

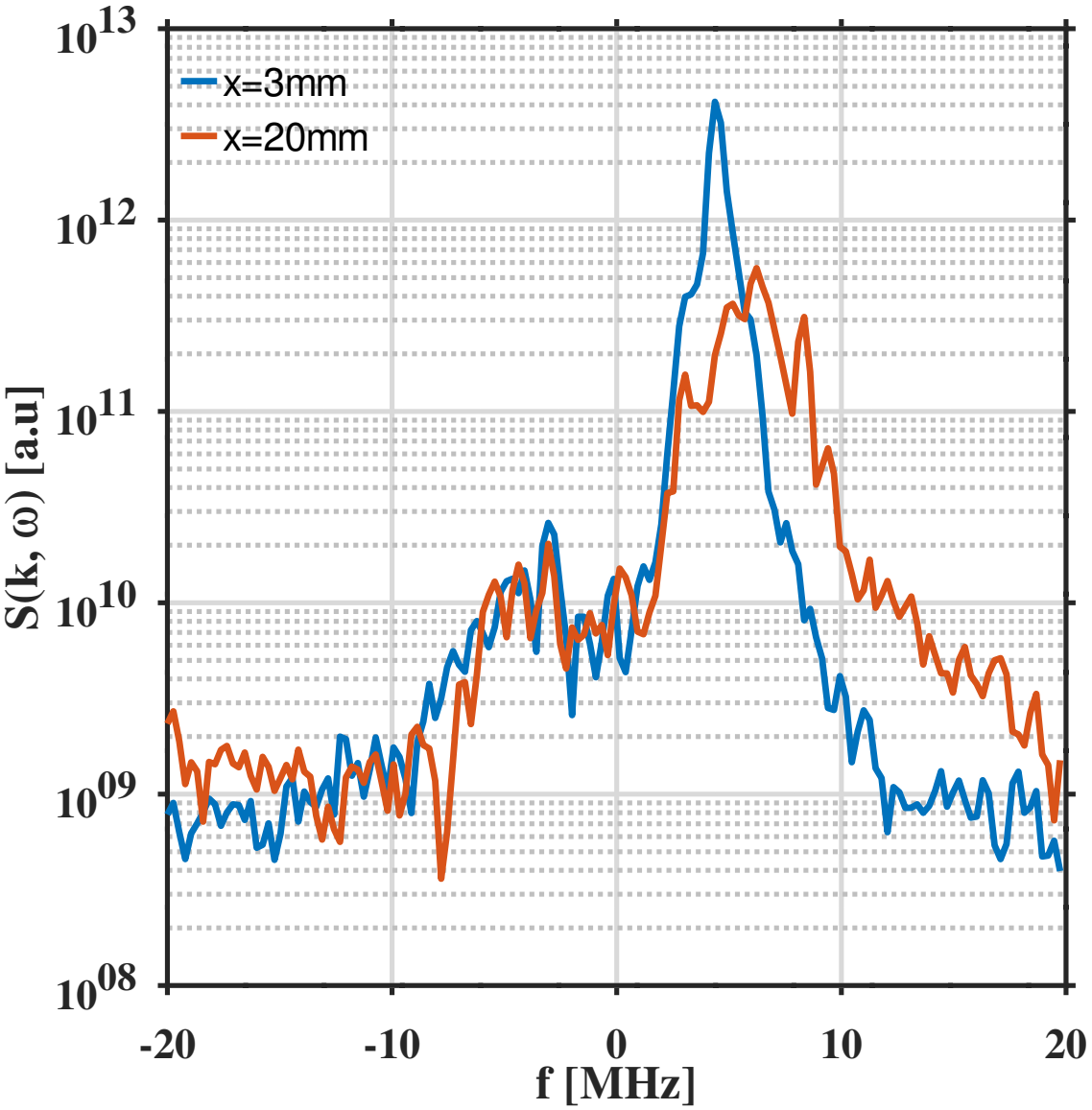

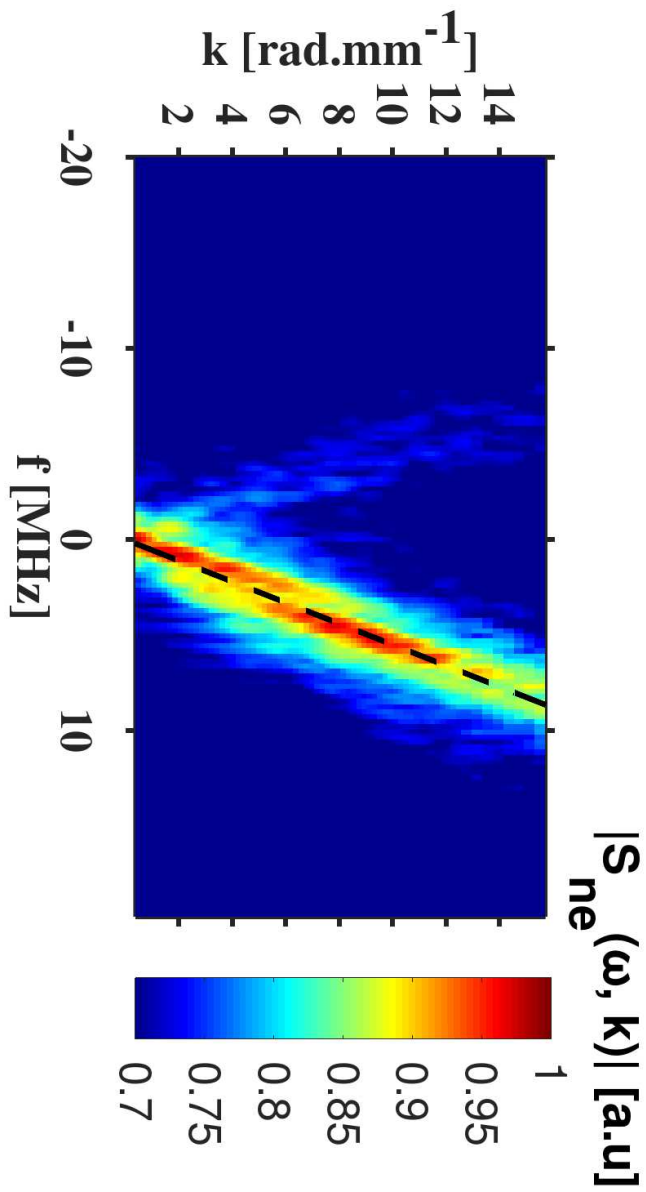

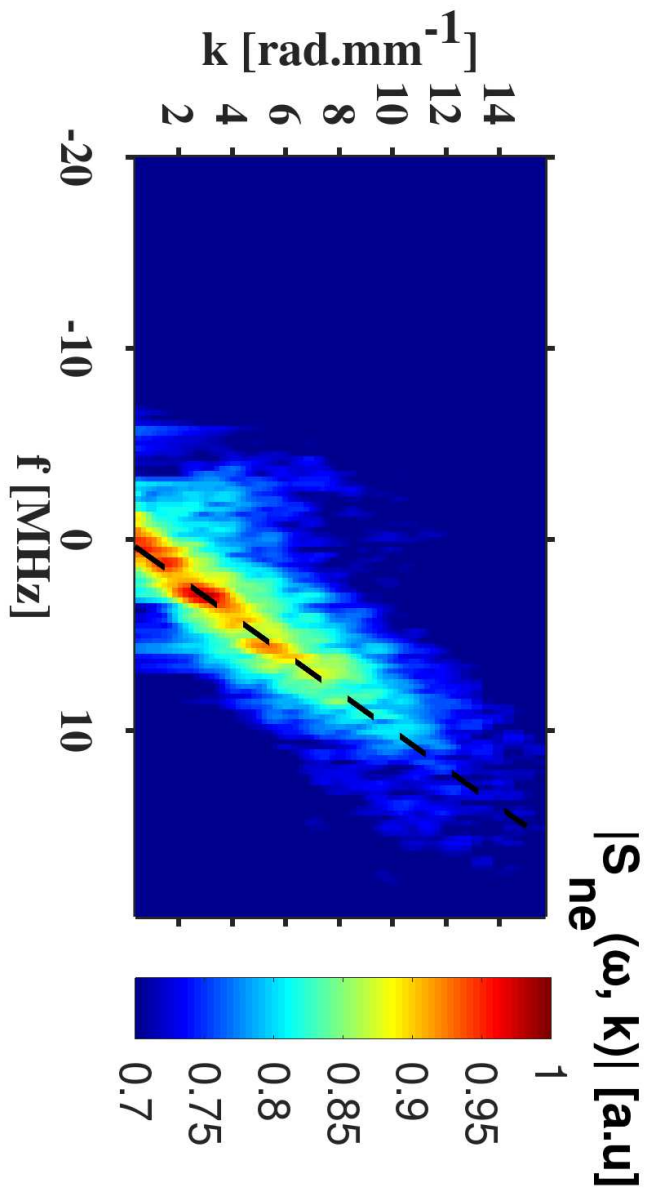

PLEASE CITE THIS ARTICLE AS DOI: 10.1063/5.0073215

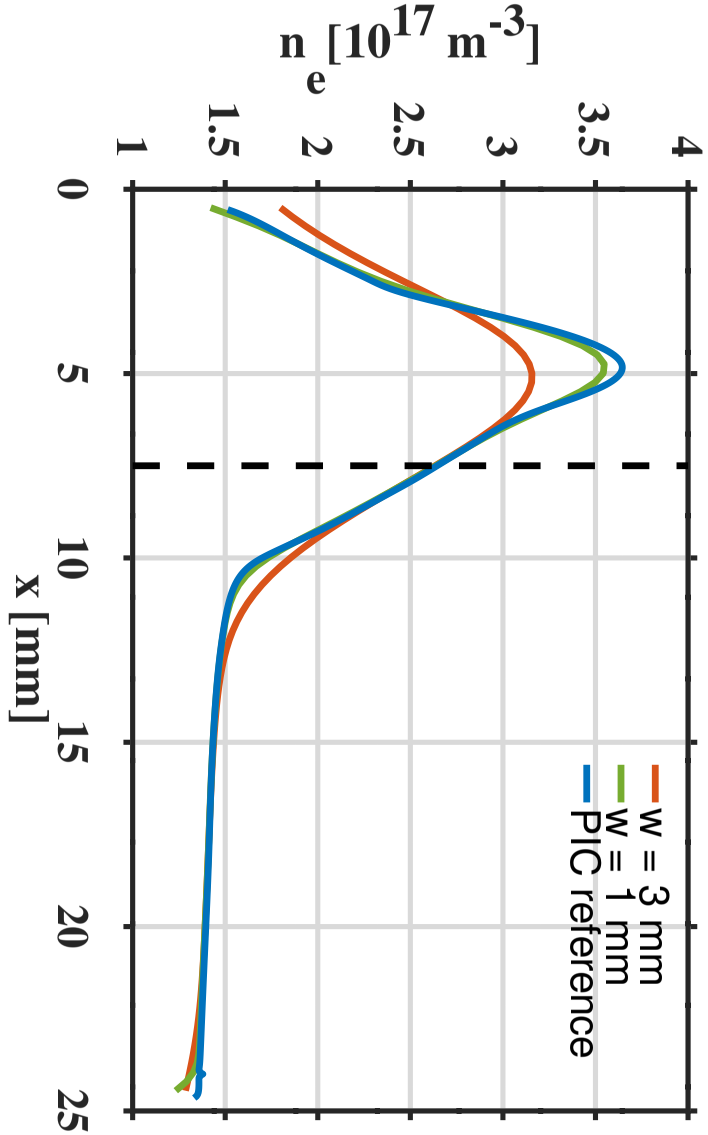

PLEASE CITE THIS ARTICLE AS DOI: 10.1063/5.0073215